Computing Non-Newtonian Fluid Flow With Radial Basis Function Networks

N. Mai-Duy* and R.I. Tanner

School of Aerospace, Mechanical and Mechatronic Engineering,

The University of Sydney, NSW 2006, Australia

Submitted to *Int. J. Numer. Meth. Fluids*, 27/9/2004; revised 17/2/2005

*Corresponding author: Telephone +61 2 9351 7151, Fax +61 2 9351 7060, E-mail nam.maiduy@aeromech.usyd.edu.au

SUMMARY

This paper is concerned with the application of radial basis function networks (RBFNs) for solving non-Newtonian fluid flow problems. Indirect RBFNs, which are based on an integration process, are employed to represent the solution variables; the governing differential equations are discretized by means of point collocation. To enhance numerical stability, stress-splitting techniques are utilized. The proposed method is verified through the computation of the rectilinear and non-rectilinear flows in a straight duct and the axisymmetric flow in an undulating tube using Newtonian, power-law, Criminale-Ericksen-Filbey (CEF) and Oldroyd-B models. The obtained results are in good agreement with the analytic and benchmark solutions.

KEY WORDS: radial basis function network; non-Newtonian fluid; straight duct; secondary flow; undulating tube.

1 Introduction

Continuum mechanics problems often lead to a set of partial differential equations (PDEs) together with a set of boundary conditions through the process of mathematical modelling. For most problems, discretization techniques are required to reduce complex systems of PDEs to systems of algebraic equations. Principal discretization methods include the finite-difference method (FDM), the finite-element method (FEM), the boundary-element method (BEM), the finite-volume method (FVM) and the spectral method. Each method has advantages over the others for certain classes of problems. They have achieved a lot of success in solving many engineering and science problems. In FEMs and FVMs, any continuous quantity is approximated by a set of piecewise continuous functions defined over a finite number of subdomains identified as elements or control volumes, i.e., mesh. Generating a mesh is still a difficult task, especially for 3D problems or even for 2D

problems with complex geometries, free surfaces or moving boundaries.

The development of numerical methods without using a mesh (meshless or meshfree methods) for the solution of PDEs has been an active research area recently. As the name suggests, there may not be any connectivity requirements between data points, leading to an easy process of numerical modelling. A comprehensive review of meshless methods can be found in [1-4]. Based on the criterion of a computational formulation, they can be divided into two categories: a) those based on the approximation of the strong form of PDEs, e.g., the smoothed particle hydrodynamics [5] and b) those based on the approximation of the weak form/inverse statement of PDEs, e.g., the reproducing kernel particle method [6]. On the other hand, based on the criterion of a mesh requirement, they can be classified into a) the so-called truly meshless methods (no mesh is involved at all), e.g., the meshless local Petrov-Galerkin method [7] and the local radial point interpolation method [8], and b) the so-called meshless methods (some mesh is still needed for either the interpolation of solution variables or the integration of weak form/inverse statement), e.g., the element free Galerkin method [9].

RBFNs, which can be regarded as scattered data approximation schemes, have found applications in many disciplines. A function to be approximated and its derivatives can be represented by direct RBFNs (DRBFNs) based on a differentiation process [10] or by indirect RBFNs (IRBFNs) based on an integration process [11]. The application of RBFNs for the numerical solution of PDEs was first reported by Kansa [12]. Since then, it has received a great deal of attention from the research community. A great number of publications are available in the literature, e.g., for a convergence proof and error bound [13], the numerical solution of potential problems [14-18], high-order differential equations [19,20], Kirchhoff plate bending problems [21] and viscous-fluid-flow problems [22,23]. In a standard RBFN-based method, all dependent variables are first approximated by global RBFNs, and the governing equations are then discretized in the strong form by point collocation. RBFNs need only a set of discrete points—instead of a set of

elements—throughout a volume, which can be randomly distributed, to approximate the field variables; hence, they can be regarded as truly meshless methods. Since RBFNs fall into the category of high-order approximation, another attractive feature lies in accuracy for a given number of data points. Furthermore, they require only a minimum amount of effort to implement.

This paper is concerned with the development of IRBFNs for the numerical solution of non-Newtonian fluid flow problems. Unlike constitutive models of Newtonian fluids, models of non-Newtonian fluids are nonlinear, making their computation difficult. For generalized Newtonian fluids, e.g., power-law fluid, the viscosity function depends on the rate of deformation of the fluid; while for viscoelastic fluids, e.g., CEF and Oldroyd-B fluids, the stress in the liquid depends not only on the present boundary data, but also on the history of the strain [24]. The present method is verified by its applications to the simulation of Newtonian, power law, CEF and Oldroyd-B fluids flowing through ducts of constant and variable cross sections that are induced by axial pressure drop. The obtained results are in good agreement with the analytic and benchmark solutions.

The remainder of the paper is organized as follows. In section 2, the governing equations are given. In section 3, the numerical formulation of non-Newtonian fluid flows using RBFNs is presented. The rectilinear and non-rectilinear flows in a straight duct and the axisymmetric flow through an indefinitely long undulating tube are simulated in section 4. Section 5 gives some concluding remarks.

2 Governing equations

Consider the flow of an incompressible fluid of density ρ and viscosity η. Any body forces are assumed negligible. The equations for the conservation of momentum and mass take

the forms

$$\rho\left(\frac{\partial \mathbf{v}}{\partial t}+\mathbf{v}.\nabla\mathbf{v}\right) = \boldsymbol{\nabla}.\boldsymbol{\sigma}, \qquad \mathbf{x}\in\Omega, \tag{1}$$

$$\nabla.\mathbf{v} = \mathbf{0}, \qquad \mathbf{x}\in\Omega, \tag{2}$$

where $\mathbf{x}$ is the position vector, t the time, Ω the domain of interest, $\mathbf{v}$ the velocity vector and $\boldsymbol{\sigma}$ the stress tensor. The stress tensor can be written as

$$\boldsymbol{\sigma} = -p\mathbf{I}+\boldsymbol{\tau}, \tag{3}$$

where p is the pressure, $\mathbf{I}$ the unit tensor and $\boldsymbol{\tau}$ the extra stress tensor. In the present work, the Newtonian, power-law, CEF and Oldroyd-B models are considered with the extra stress tensors defined as

$$\boldsymbol{\tau} = \eta\dot{\boldsymbol{\gamma}}, \qquad \text{(Newtonian model)}, \tag{4}$$

$$\boldsymbol{\tau} = \eta(\dot{\gamma})\dot{\boldsymbol{\gamma}},\ \eta(\dot{\gamma}) = k|\dot{\gamma}|^{n-1}, \qquad \text{(power-law model)}, \tag{5}$$

$$\boldsymbol{\tau} = \eta(\dot{\gamma})\dot{\boldsymbol{\gamma}} - \frac{1}{2}\Psi_1\frac{\Delta\dot{\boldsymbol{\gamma}}}{\Delta t}+\Psi_2\dot{\boldsymbol{\gamma}}.\dot{\boldsymbol{\gamma}},\ \eta(\dot{\gamma}) = k|\dot{\gamma}|^{n-1}, \qquad \text{(CEF model)}, \tag{6}$$

$$\boldsymbol{\tau} = \eta_s\dot{\boldsymbol{\gamma}}+\mathbf{S},\ \mathbf{S}+\lambda\frac{\Delta\mathbf{S}}{\Delta t} = \eta\dot{\boldsymbol{\gamma}}, \qquad \text{(Oldroyd-B model)}, \tag{7}$$

where $\dot{\boldsymbol{\gamma}}$ is the rate of deformation tensor,

$$\dot{\boldsymbol{\gamma}} = \nabla\mathbf{v}+\nabla\mathbf{v}^T;$$

$\dot{\gamma}$ is the scalar magnitude of $\dot{\boldsymbol{\gamma}}$,

$$\dot{\gamma} = \sqrt{(1/2)\mathrm{tr}(\dot{\boldsymbol{\gamma}}.\dot{\boldsymbol{\gamma}})},$$

in which "tr" denotes the trace operation; k the consistency factor; n the power-law index; Ψ_1 and Ψ_2 the first and second normal stress coefficients, respectively; $\eta_s\dot{\boldsymbol{\gamma}}$ the

solvent-contributed stress (η_s the solvent viscosity); $\mathbf{S}$ the polymer-contributed stress; λ the relaxation time; and $\frac{\Delta[]}{\Delta t}$ the upper convected derivative,

$$\frac{\Delta[]}{\Delta t} = \frac{\partial[]}{\partial t} + (\mathbf{v}.\nabla)[] - \nabla\mathbf{v}^T.[] - [].\nabla\mathbf{v}.$$

3 Radial basis function networks

A function y, to be approximated, can be represented by an RBFN as follows [25]

$$y(\mathbf{x}) \approx f(\mathbf{x}) = \sum_{i=1}^{m} w^{(i)} g^{(i)}(\mathbf{x}), \tag{8}$$

where superscript denotes the elements of an RBFN, $\mathbf{x}$ the input vector, m the number of RBFs, $\{w^{(i)}\}_{i=1}^{m}$ the set of network weights to be found, and $\{g^{(i)}(\mathbf{x})\}_{i=1}^{m}$ the set of RBFs.

According to Micchelli's theorem, there is a large class of RBFs, e.g., multiquadrics, inverse multiquadrics and Gaussian functions, whose design matrices (interpolation matrices) obtained from (8) are always invertible provided that the data points are distinct. This is all that is required for nonsingularity of design matrices, whatever the number of data points and the dimension of problem [26,25]. It has been proved that RBFNs are capable of representing any continuous function to a prescribed degree of accuracy in the L_p norm, $p \in [1, \infty]$ [27,25]. On the other hand, according to the Cover theorem, the higher the number of neurons (RBFs) used, the more accurate the approximation will be [28], indicating the property of "mesh convergence" of RBFNs. These important theorems can be seen to provide the theoretical basis for the design of RBFNs to the field of numerical solution of PDEs.

In solving PDEs with RBFNs, multiquadrics (MQ) and thin plate splines (TPS) are widely applied. MQs are the most widely used since several experiments have shown that, in

general, they tend to result in the most accurate approximation. The MQ-approximation scheme gives exponential convergence with the refinement of spatial discretization. In practice, the MQ-RBFN solution can be strongly influenced by the RBF width (shape parameter), and how to choose the best value of this free parameter is still open. On the other hand, TPSs do not involve the adjustable shape parameter. Like the MQ case, high accuracy can be obtained using relatively low data densities. However, TPSs possess only linear convergence [18]. In the present work, these RBFs are implemented, whose forms are

$$g^{(i)}(\mathbf{x}) = \sqrt{(\mathbf{x}-\mathbf{c}^{(i)})^T(\mathbf{x}-\mathbf{c}^{(i)}) + a^{(i)2}} \quad \text{(MQ)}, \tag{9}$$

$$g^{(i)}(\mathbf{x}) = (\mathbf{x}-\mathbf{c}^{(i)})^T(\mathbf{x}-\mathbf{c}^{(i)}) \log\left(\sqrt{(\mathbf{x}-\mathbf{c}^{(i)})^T(\mathbf{x}-\mathbf{c}^{(i)})}\right) \quad \text{(TPS)}, \tag{10}$$

where $\mathbf{c}^{(i)}$ and $a^{(i)}$ are the centre and the width of the ith RBF, respectively, and superscript T denotes the transpose of a vector. To make the training process simple, the set of centres is chosen to be the same as the set of collocation points, i.e., $\{\mathbf{c}^{(i)}\}_{i=1}^{m} \equiv \{\mathbf{x}^{(i)}\}_{i=1}^{p}$ with $m = p$, and the width $a^{(i)}$ is computed using the following relation

$$a^{(i)} = \beta d^{(i)}, \tag{11}$$

where β is a positive scalar and $d^{(i)}$ is the minimum of distances from the ith center to its neighbours. Relation (11) allows the MQ width a to be broader in the area of lower data density and narrower in the area of higher data density in order to achieve a certain amount of response overlap between each RBF and its neighbours ("P nearest neighbour" heuristics) ([15] and references therein).

3.1 Direct approach

In the DRBFN approach, the RBFN (8) is utilized to represent the original function y; subsequently, its derivatives are computed by differentiating (8) as

$$y(\mathbf{x}) \approx f(\mathbf{x}) = \sum_{i=1}^{m} w^{(i)} g^{(i)}(\mathbf{x}), \tag{12}$$

$$\frac{\partial y(\mathbf{x})}{\partial x_j} \approx \frac{\partial f(\mathbf{x})}{\partial x_j} = \frac{\partial \left(\sum_{i=1}^{m} w^{(i)} g^{(i)}(\mathbf{x}) \right)}{\partial x_j} = \sum_{i=1}^{m} w^{(i)} h^{(i)}(\mathbf{x}), \tag{13}$$

$$\frac{\partial^2 y(\mathbf{x})}{\partial x_j^2} \approx \frac{\partial^2 f(\mathbf{x})}{\partial x_j^2} = \frac{\partial \left(\sum_{i=1}^{m} w^{(i)} h^{(i)}(\mathbf{x}) \right)}{\partial x_j} = \sum_{i=1}^{m} w^{(i)} \bar{h}^{(i)}(\mathbf{x}), \tag{14}$$

where subscript j denotes the scalar components of a vector; $h^{(i)}(\mathbf{x}) = \partial g^{(i)}(\mathbf{x})/\partial x_j$ and $\bar{h}^{(i)}(\mathbf{x}) = \partial h^{(i)}(\mathbf{x})/\partial x_j$ are new derived basis functions for the approximation of the first- and the second-order derivatives of the original function y, respectively.

3.2 Indirect approach

In this approach, RBFNs are used to represent the highest-order derivatives of a function y, e.g., $\partial^2 y/\partial x_1^2$ and $\partial^2 y/\partial x_2^2$—the highest ones under consideration here. Lower-order derivatives and finally the function itself are then obtained by integrating those RBFNs as follows

$$\frac{\partial^2 y(\mathbf{x})}{\partial x_j^2} \approx \frac{\partial^2 f(\mathbf{x})}{\partial x_j^2} = \sum_{i=1}^{m} w_{[x_j]}^{(i)} g^{(i)}(\mathbf{x}), \tag{15}$$

$$\frac{\partial y(\mathbf{x})}{\partial x_j} \approx \frac{\partial f(\mathbf{x})}{\partial x_j} = \sum_{i=1}^{m+q_1} w_{[x_j]}^{(i)} H_{[x_j]}^{(i)}(\mathbf{x}), \tag{16}$$

$$y(\mathbf{x}) \approx f(\mathbf{x}) = \sum_{i=1}^{m+q_2} w_{[x_j]}^{(i)} \bar{H}_{[x_j]}^{(i)}(\mathbf{x}). \tag{17}$$

where subscripts $[x_j]$ denote the quantities resulting from the process of integration in the x_j direction; q_1 the number of new centres in a subnetwork that is employed to

approximate a set of nodal integration constants; $q_2 = 2q_1$; $H^{(i)}_{[x_j]} = \int g^{(i)} dx_j$ and $\bar{H}^{(i)}_{[x_j]} = \int H^{(i)} dx_j$ $(i = 1, 2, \cdots, m)$ are new derived basis functions for the approximation of the first-order derivative and the original function y, respectively. For convenience of presentation, the new centres and their associated known basis functions in subnetworks are also denoted by the notations $w^{(i)}$ and $H^{(i)}(\mathbf{x})$ $(\bar{H}^{(i)}(\mathbf{x}))$, respectively, but with $i > m$.

Since integration is a smoothing operation, the approximating functions obtained by the IRBFN method are expected to be much smoother than those by the DRBFN method. Previous findings showed that the former performs better than the latter in terms of accuracy and convergence rate [11].

The theoretical justification for applying RBFNs to solve general PDEs with RBFNs has not been established yet [17]. Recently, Franke and Schaback [13] gave a convergence proof and error bound for methods solving constant-coefficient PDEs by collocation using DRBFNs. A formal theoretical proof of the superior accuracy of the IRBFN method and the non-singularity of IRBFN matrices cannot be offered at this stage.

Unlike FEMs and BEMs, where the integration process is used to reduce the order of the continuity required for the variables, the integration process in the IRBFN method is employed solely to obtain new basis functions from RBFs. In the context of meshless methods, all relevant integrals in the IRBFN method using MQs and TPSs are determined analytically, leading directly to a truly meshless method; while the integration of the weak form associated with FEM or the inverse statement associated with BEM must be computed numerically, and hence they require some special treatments, e.g., using local weak form/local inverse statement, to achieve a mesh-free feature.

When the problem dimension N is greater than 1, the size of a system of equations obtained by the IRBFN approach is about N times as big as that by the DRBFN approach. Thus, it is necessary to make a prior conversion of the multiple spaces of network weights into the single space of function values to overcome this drawback.

The evaluation of (15)-(17) at a set of collocation points $\{\mathbf{x}^{(k)}\}_{k=1}^{m}$ yields

$$\mathbf{f}_{,\mathbf{jj}} = \mathbf{G}\mathbf{w}_{[x_j]}, \tag{18}$$

$$\mathbf{f}_{,\mathbf{j}} = \mathbf{H}_{[x_j]}\mathbf{w}_{[x_j]}, \tag{19}$$

$$\mathbf{f} = \bar{\mathbf{H}}_{[x_j]}\mathbf{w}_{[x_j]}, \tag{20}$$

where $\mathbf{G}$, $\mathbf{H}$ and $\bar{\mathbf{H}}$, whose rows can be seen in (28), (27) and (26), are the design matrices associated with the approximation of the second-order derivative, the first-order derivative, and the function, respectively; $\mathbf{w}_{[x_j]}$ the set of network weights in the x_j direction to be found; $\mathbf{f} = \{f(\mathbf{x}^{(k)})\}_{k=1}^{m}$; $\mathbf{f}_{,\mathbf{j}} = \{\frac{\partial f(\mathbf{x}^{(k)})}{\partial x_j}\}_{k=1}^{m}$ and $\mathbf{f}_{,\mathbf{jj}} = \{\frac{\partial^2 f(\mathbf{x}^{(k)})}{\partial x_j^2}\}_{k=1}^{m}$. For the purpose of computation, the two matrices $\mathbf{G}$ and $\mathbf{H}$ are augmented using zero-submatrices so that they have the same size as the matrix $\bar{\mathbf{H}}$. By solving (20) using the general linear least squares method, the set of network weights can be expressed in terms of the nodal function values as

$$\mathbf{w}_{[x_j]} = \bar{\mathbf{H}}_{[x_j]}^{-1}\mathbf{f}, \tag{21}$$

where $\bar{\mathbf{H}}_{[x_j]}^{-1}$ is the Moore-Penrose pseudoinverse, and the dimensions of $\mathbf{w}$, $\bar{\mathbf{H}}_{[x_j]}^{-1}$ and $\mathbf{f}$ are respectively $(m + q_2) \times 1$, $(m + q_2) \times m$ and $m \times 1$. Substitution of (21) into (18)-(20) yields

$$\mathbf{f}_{,\mathbf{jj}} = \mathbf{G}\bar{\mathbf{H}}_{[x_j]}^{-1}\mathbf{f}, \tag{22}$$

$$\mathbf{f}_{,\mathbf{j}} = \mathbf{H}_{[x_j]}\bar{\mathbf{H}}_{[x_j]}^{-1}\mathbf{f}, \tag{23}$$

$$\mathbf{f} = \bar{\mathbf{H}}_{[x_j]}\bar{\mathbf{H}}_{[x_j]}^{-1}\mathbf{f}. \tag{24}$$

Cross derivatives $\partial f^2(\mathbf{x})/\partial x_i \partial x_j$ can be straightforwardly computed by using the design matrices associated with the first-order derivatives (23). Although the order of differentiation makes no difference, it would be better to take the average due to numerical

error,

$$\begin{aligned}\frac{\partial^2 f}{\partial x_i \partial x_j} &= \frac{1}{2}\left(\frac{\partial}{\partial x_i}\left(\frac{\partial f}{\partial x_j}\right)+\frac{\partial}{\partial x_j}\left(\frac{\partial f}{\partial x_i}\right)\right),\\ \mathbf{f_{,ij}} &= \frac{1}{2}\left(\mathbf{H}_{[x_i]}\bar{\mathbf{H}}^{-1}_{[x_i]}\left(\mathbf{H}_{[x_j]}\bar{\mathbf{H}}^{-1}_{[x_j]}\mathbf{f}\right)+\mathbf{H}_{[x_j]}\bar{\mathbf{H}}^{-1}_{[x_j]}\left(\mathbf{H}_{[x_i]}\bar{\mathbf{H}}^{-1}_{[x_i]}\mathbf{f}\right)\right). \qquad (25)\end{aligned}$$

Expressions of f and its derivatives at an arbitrary point $\mathbf{x}$ can be given by

$$f(\mathbf{x}) = \frac{1}{N}\sum_{j=1}^{N}\left(\left[\bar{H}^{(1)}_{[x_j]}(\mathbf{x}),\cdots,\bar{H}^{(m+1)}_{[x_j]}(\mathbf{x}),\cdots,\bar{H}^{(m+q_1+1)}_{[x_j]}(\mathbf{x}),\cdots\right]\bar{\mathbf{H}}^{-1}_{[x_j]}\mathbf{f}\right), \qquad (26)$$

$$\frac{\partial f(\mathbf{x})}{\partial x_j} = \left[H^{(1)}_{[x_j]}(\mathbf{x}),\cdots,H^{(m+1)}_{[x_j]}(\mathbf{x}),\cdots,0,\cdots\right]\bar{\mathbf{H}}^{-1}_{[x_j]}\mathbf{f}, \qquad (27)$$

$$\frac{\partial^2 f(\mathbf{x})}{\partial x_j^2} = \left[g^{(1)}_{[x_j]}(\mathbf{x}),\cdots,0,\cdots,0,\cdots\right]\bar{\mathbf{H}}^{-1}_{[x_j]}\mathbf{f}, \qquad (28)$$

$$\begin{aligned}\frac{\partial^2 f(\mathbf{x})}{\partial x_i \partial x_j} = \frac{1}{2}(&\left[H^{(1)}_{[x_i]}(\mathbf{x}),\cdots,H^{(m+1)}_{[x_i]}(\mathbf{x}),\cdots,0,\cdots\right]\bar{\mathbf{H}}^{-1}_{[x_i]}\left(\mathbf{H}_{[x_j]}\bar{\mathbf{H}}^{-1}_{[x_j]}\mathbf{f}\right)\\ &+\left[H^{(1)}_{[x_j]}(\mathbf{x}),\cdots,H^{(m+1)}_{[x_j]}(\mathbf{x}),\cdots,0,\cdots\right]\bar{\mathbf{H}}^{-1}_{[x_j]}\left(\mathbf{H}_{[x_i]}\bar{\mathbf{H}}^{-1}_{[x_i]}\mathbf{f}\right)), \qquad (29)\end{aligned}$$

where N is the dimension of the problem. In (26), the approximate function f at $\mathbf{x}$ is taken to be the average value of $f_{[x_j]}(\mathbf{x})$'s due to numerical error.

From (26)-(29), a function y and its derivatives are now expressed in terms of function values rather than in terms of network weights. As a result, in solving PDEs, the present IRBFN method leads to a system of equations whose size is approximately equal to that of the DRBFN method, irrespective of the problem dimension. The process of transforming network-weight space into physical space completely eliminates the problem of the large system/final-matrix size of the IRBFN method. However, the IRBFN method requires more work than the DRBFN method.

3.3 The numerical IRBFN formulation

Each dependent variable and its derivatives in the governing equations (1)-(7) can be approximated by RBFNs using either (12)-(14) for the DRBFN approach or (26)-(29) for the IRBFN approach. The closed-form representations obtained are substituted into the governing equations, and the system of PDEs is then discretized by means of point collocation. The RBFN solution thus satisfies the governing equations pointwise rather than in an average sense. In the present work, only the IRBFN approach is employed. In contrast to previous works dealing with potential and viscous flow problems [15,22], the present IRBFN formulation is expressed in terms of the nodal variable values. For the elliptic momentum equations, one only needs to enforce these equations at interior points because the velocity boundary conditions are prescribed along the entire boundary. For the hyperbolic constitutive equations, the IRBFN formulation is demonstrated through one equation in (7), e.g., for S_{zz},

$$\begin{aligned}
&\sum_{i=1}^{nip}\{S_{zz}^{(i)} + \lambda(v_r^{(i)} \sum_{j=1}^{m} \left(\mathbf{H}_{[r]}\bar{\mathbf{H}}_{[r]}^{-1}\right)_{[i,j]} S_{zz}^{(j)} + v_z^{(i)} \sum_{j=1}^{m} \left(\mathbf{H}_{[z]}\bar{\mathbf{H}}_{[z]}^{-1}\right)_{[i,j]} S_{zz}^{(j)} \\
&- 2S_{rz}^{(i)} \sum_{j=1}^{m} \left(\mathbf{H}_{[r]}\bar{\mathbf{H}}_{[r]}^{-1}\right)_{[i,j]} v_z^{(j)} - 2S_{zz}^{(i)} \sum_{j=1}^{m} \left(\mathbf{H}_{[z]}\bar{\mathbf{H}}_{[z]}^{-1}\right)_{[i,j]} v_z^{(j)}) \\
&- 2\eta \sum_{j=1}^{m} \left(\mathbf{H}_{[z]}\bar{\mathbf{H}}_{[z]}^{-1}\right)_{[i,j]} v_z^{(j)}\}^2 \to 0,
\end{aligned} \tag{30}$$

where (r, θ, z) denotes the cylindrical polar coordinates, nip the number of interior points, m the number of centres excluding centres on the tube wall and $[i, j]$ the element located at row i and column j of a matrix. On the tube wall, (7) is reduced to a set of algebraic equations because of $\Delta\mathbf{S}/\Delta t = 0$; consequently, the stress components can be easily computed. In this regard, for solving hyperbolic equations, one may not need to include the tube-wall points in the set of centres. Other equations in (7) can be discretized in a similar fashion. The IRBFN discretization leads to a square system of equations.

4 Numerical examples

Axial-pressure-drop-induced flows in a straight duct and in a "wiggly" tube using Newtonian, power-law, CEF and Oldroyd-B fluid models are simulated to study the performance of the IRBFN method,.

4.1 Rectilinear and non-rectilinear flows in a straight duct

MQs are employed to compute flows of a power-law fluid through circular and non-circular tubes, while TPSs are used to simulate the flow of a viscoelastic fluid through a square duct. For simplicity, in the MQ-based approximation scheme, the factor β is chosen to be unity. To enhance numerical stability, a stress-splitting formulation is employed. The resulting nonlinear system of equations is solved by a decoupled approach, where a Picard-type iteration scheme is utilized to render nonlinear terms linear. At each iteration, a perturbed Newtonian problem and a constitutive model are solved in two sequential steps. For a given kinematics, a pseudo-body force field is obtained by solving the constitutive model. The kinematics are then updated by solving the momentum and the continuity equations. The procedure is iterated until a stopping criterion is satisfied. Hence, an attractive feature of this technique lies in the small requirement of computer memory. For low values of n, it is necessary to relax the iterative process by applying a relaxation factor to the field variables according to, e.g., for a component velocity v_j,

$$v_j = \alpha v_j^{(k)} + (1-\alpha) v_j^{(k-1)}, \tag{31}$$

where α is the relaxation factor ($0 < \alpha \leq 1$) and superscript k indicates the current iteration. Convergence measure (CM) at the kth iteration is defined as

$$CM = \sqrt{\frac{\sum_{j=1}^{N}\sum_{i=1}^{m}\left[v_j^k(\mathbf{x}^{(i)}) - v_j^{k-1}(\mathbf{x}^{(i)})\right]^2}{\sum_{j=1}^{N}\sum_{i=1}^{m}\left[v_j^k(\mathbf{x}^{(i)}))\right]^2}},$$

where N is the problem dimension and m the number of collocation points.

4.1.1 Fully developed laminar flow of power-law fluid in a straight circular pipe

For the flow of a power-law fluid in a straight circular pipe ($v_r = 0;\ v_\theta = 0;\ v_z = v_z(r)$), the continuity equation (2) is automatically satisfied, and the momentum equation (1) can be reduced to

$$\frac{1}{r}\frac{\partial}{\partial r}\left(\eta r \frac{\partial v_z}{\partial r}\right) - \frac{\partial p}{\partial z} = 0, \tag{32}$$

$$\eta = k\left|\frac{\partial v_z}{\partial r}\right|^{n-1}, \tag{33}$$

on the domain $0 < r < R$, which is solved subject to the boundary conditions

$$\frac{\partial v_z}{\partial r} = 0, \quad \text{at} \quad r = 0, \tag{34}$$

$$v_z = 0, \quad \text{at} \quad r = R. \tag{35}$$

The exact solution of this problem is

$$v_{ze} = \frac{n}{n+1}\left(\frac{-\partial p/\partial z}{2k}\right)^{1/n} R^{(n+1)/n}\left[1 - \left(\frac{r}{R}\right)^{(n+1)/n}\right].$$

Since the exact solution is available, the accuracy of a numerical solution can be measured via the norm of relative errors of the solution as follows

$$N_e = \sqrt{\frac{\sum_{i=1}^{m} \left[v_{ze}(x^{(i)}) - v_z(x^{(i)})\right]^2}{\sum_{i=1}^{m} v_{ze}(x^{(i)})^2}}, \tag{36}$$

where v_z and v_{ze} are the calculated and the exact solutions, respectively.

The governing equation (32) can be rewritten as

$$\eta \frac{\partial^2 v_z}{\partial r^2} + \frac{\partial \eta}{\partial r}\frac{\partial v_z}{\partial r} - \frac{\partial p}{\partial z} + \frac{\eta}{r}\frac{\partial v_z}{\partial r} = 0. \tag{37}$$

This equation is widely used in FDMs. For generalized Newtonian fluids, the viscosity η is a function of the velocity field. As a result, a system matrix obtained from (37) varies and needs to be inverted at each iteration.

The power-law fluid implies an infinite viscosity when the shear rate $\dot{\gamma}$ vanishes; some special treatments for terms involving η are required. Young and Wheeler [29] treated this infinity by using a truncation procedure. A large value of the viscosity, namely η_{max}, is given. If η does not exceed η_{max}, then the computed value is accepted. Otherwise, η is set equal to η_{max}. For collocation methods, one can simply treat this singularity by not applying the governing equations at points of infinite viscosity. In the present work, the extra stress tensor is decomposed into two components

$$\boldsymbol{\tau} = \left([\eta - \eta_0] + \eta_0\right)\dot{\boldsymbol{\gamma}} = [\eta - \eta_0]\dot{\boldsymbol{\gamma}} + \eta_0\dot{\boldsymbol{\gamma}}. \tag{38}$$

It is obvious that η_0 can be chosen arbitrarily. Substitution of (38) into (32) yields

$$\eta_0\left(\frac{\partial^2 v_z}{\partial r^2} + \frac{1}{r}\frac{\partial v_z}{\partial r}\right) - \frac{\partial p}{\partial z} + \left(\frac{\partial}{\partial r}\left([\eta - \eta_0]\frac{\partial v_z}{\partial r}\right) + \frac{[\eta - \eta_0]}{r}\frac{\partial v_z}{\partial r}\right) = 0, \tag{39}$$

in which the last two terms on the left-hand side can be regarded as a pseudo-body force.

A system matrix obtained from (39) depends only on the geometry and hence needs to be inverted only once.

The question here is how to choose an optimum η_0. Two studies are conducted. Firstly, η_0 is chosen to be the Newtonian-like viscosity corresponding to $n = 1$ ($\eta_0 = \eta_N = k$); secondly, η_0 is taken to be the average viscosity of the previous iteration ($\eta_0 = \bar{\eta}$). Numerical experience shows that the case $\eta_0 = \bar{\eta}$ outperforms the case $\eta_0 = \eta_N$ regarding the convergence behaviour of an iterative procedure (Figure 1) and the achievement of a low-power-law-index solution.

A wide range of n varying from 1 to 1/5 is considered. All values of k, $-\partial p/\partial z$ and R are chosen to be unity. The obtained results are displayed in Figure 2, where the velocity component v_z is normalized with the average velocity $\bar{v}_z = 2\pi \int_0^1 r v_z(r) dr$ in which the integral is computed using Simpson rule. Good agreement is seen between the exact and the computed solutions. For example, at $n = 1/5$, the method achieves a small error-norm, $N_e = 6.4e-4$, using 13 collocation points. "Mesh convergence" is shown in Figure 3, where the IRBFN solution converges apparently as $O(h^{3.85})$ in which h is the centre spacing. As mentioned earlier, the MQ width can critically affect the performance of MQ-RBFNs. However, there is no general theory yet for determining the best value of the MQ width. Consequently, in practice, it is difficult to achieve exponential convergence, even for the case of function approximation.

4.1.2 Fully developed laminar flow of power-law fluid in a square duct

Computing the flow in a square duct is known to be more complicated than computing the flow in a circular pipe flow. A two-dimensional computation is required. For non-Newtonian fluids, exact solutions are not available; one needs to resort to numerical methods. Hartnett and Kostic [30] gave a comprehensive review on the heat transfer behaviour and the friction factor of the generalized-Newtonian-fluid flow through a rect-

angular duct. The flow was simulated by a number of numerical methods, for example, a variational principle [31], FDM [32] and FEM[33]. It was indicated that convergence often fails for $n < 0.4$.

It is plausible to assume that the flow of an inelastic fluid in a straight duct is rectilinear, i.e., $v_x = 0, v_y = 0$ and $v_z = v_z(x, y)$. The governing equations (1)-(3) and (5) can be reduced to

$$\frac{\partial}{\partial x}\left(\eta\frac{\partial v_z}{\partial x}\right) + \frac{\partial}{\partial y}\left(\eta\frac{\partial v_z}{\partial y}\right) - \frac{\partial p}{\partial z} = 0, \tag{40}$$

$$\eta = k\left[\left(\frac{\partial v_z}{\partial x}\right)^2 + \left(\frac{\partial v_z}{\partial y}\right)^2\right]^{\frac{n-1}{2}}. \tag{41}$$

A stress-splitting formulation is employed here to enhance numerical stability and reduce computational effort. Owing to the symmetry, only a quarter of the 2D domain is considered (Figure 4). The domain of interest, $\partial p/\partial z$ and k are chosen to be 0.5×0.5, -1 and 1, respectively. Special attention is given to the treatment for the Neumann condition $\partial v_z/\partial \bar{n}$ ($\bar{n}$ the coordinate normal to the boundary). The present method implements this type of boundary condition as follows. Along the two sides $x = 0$ and $y = 0$, normal derivatives $\partial v_z/\partial \bar{n}$ are given, and hence the task now is to express the nodal values of v_z along these sides in terms of the interior nodal variable values. This can be achieved by solving the following subsystem of equations

$$\frac{\partial v_z(\mathbf{x}^{(i)})}{\partial \bar{n}} = \sum_{j=1}^{m}\left(\mathbf{H}_{[x_n]}\bar{\mathbf{H}}^{-1}_{[x_n]}\right)_{[i,j]} v_z^{(j)}, \tag{42}$$

where $\mathbf{x}^{(i)} = \{(x = 0, y), (x, y = 0)\}$. Making use of the results obtained from (42) and the Dirichlet condition ($v_z = 0$ along the wall), a square system of equations is obtained with the unknowns being only the interior variable values. Once the system of equations is solved, a numerical solution v_z along these two sides ($x = 0$ and $y = 0$) may be found from (42).

Again, the case $\eta_0 = \bar{\eta}$ yields faster convergence than the case $\eta_0 = \eta_N$. For example, at $n = 0.8$ and $\alpha = 0.1$, it takes about 10 and 35 iterations to obtain convergence ($CM < 1.e-6$) for $\eta_0 = \bar{\eta}$ and $\eta_0 = \eta_N$, respectively. Furthermore, low values of n, at least $1/5$, are simulated successfully with the former, while the latter is only able to obtain convergence for $1 \geq n \geq 0.4$. Due to the fact that the solving procedure is Picard-type iterative, an initial solution can greatly affect convergence behaviour. Here, the computed solutions at greater values of n are chosen to be initial solutions. Figure 5 presents the plot of convergence measure versus iteration for several initial solutions. It can be seen that a closer initial solution yields faster convergence.

Another important quantity associated with this type of flow is the friction factor-Reynolds number product, termed fRe, which describes the relationship between flow rate and pressure drop. For the problem under consideration, the quantity fRe has the form

$$fRe = \frac{1}{2\bar{v}_z^n}, \tag{43}$$

where $\bar{v}_z$ is the average velocity in the flow direction, defined as

$$\bar{v_z} = 4 \int_0^{0.5} \int_0^{0.5} v_z(x, y) dx dy,$$

in which the double integral can be evaluated using Simpson quadrature. Based on the Rabinowitsch-Mooney equation, Kozicki, Chou and Tiu [34] derived an approximate expression of the friction factor defined as, e.g., for a square duct,

$$fRe = 2^{3n+1} \left(0.6771 + \frac{0.2121}{n} \right)^n.$$

Results for the friction factor obtained by the present method and other methods [31-34] are summarized in Table 1. These predictions are in good agreement over a wide range of n. The maximum relative error between IRBFN and FEM is less than 0.7%.

4.1.3 Fully developed flow of viscoelastic fluid in a square duct

Viscoelastic fluids possess both viscous and elastic properties. For the fully developed flow of a viscoelastic fluid through a straight duct, the second normal stress difference is expected to generate some secondary flow which is transverse to the main flow along the axis of a duct. However, it does not happen for all cases [24]. For example, the flow is still rectilinear if the slip surfaces are parallel planes or coaxial circular cylinders; or if the second normal stress coefficient (Ψ_2) is a constant multiple of the viscosity function. Nevertheless, the appearance of transverse circulations can be seen as a distinguishing feature of viscoelastic fluids relative to inelastic fluids. As a result, much attention is paid to the investigation of the development of secondary motions. In earlier studies, Green and Rivlin [35] examined the flow in a tube of elliptical cross-section, using a special constitutive equation, and found a weak secondary circulation in each quadrant, whereas Langlois and Rivlin [36] extended this work for a more general class of fluids. The secondary flow in a rectangular duct was then studied extensively, for example, using perturbation approximation [37], FVM [38,39], FDM [40] and FEM [41].

For the purpose of validating the IRBFN method, the present work considers the flow of a 2% viscarin solution in distilled water through a straight duct of square cross-section that was studied numerically and experimentally by Gervang and Larson [38]. In view of the fact that the secondary flow is weak, i.e., the transverse velocity components are small relative to the main axial velocity component, the fluid can be modelled by the CEF equation for which rheometric functions are available:

$$\eta = k\dot{\gamma}^{n-1},\ k = 8.5\ Pas^n,\ n = 0.37,$$

$$\Psi_1 = k_1\dot{\gamma}^{n_1},\ k_1 = 5.96\ Pas^{n_1+2},\ n_1 = -1.35,$$

$$\Psi_2 = -0.15\Psi_1.$$

Since the fully developed flow is independent of the streamwise coordinate, the governing equations in a stress-splitting form can be reduced to

$$\rho\left(v_x\frac{\partial v_x}{\partial x}+v_y\frac{\partial v_x}{\partial y}\right) = -\frac{\partial p}{\partial x}+\eta_0\left(\frac{\partial^2 v_x}{\partial x^2}+\frac{\partial^2 v_x}{\partial y^2}\right)+\frac{\partial S_{xx}}{\partial x}+\frac{\partial S_{xy}}{\partial y}, \tag{44}$$

$$\rho\left(v_x\frac{\partial v_y}{\partial x}+v_y\frac{\partial v_y}{\partial y}\right) = -\frac{\partial p}{\partial y}+\eta_0\left(\frac{\partial^2 v_y}{\partial x^2}+\frac{\partial^2 v_y}{\partial y^2}\right)+\frac{\partial S_{yx}}{\partial x}+\frac{\partial S_{yy}}{\partial y}, \tag{45}$$

$$\rho\left(v_x\frac{\partial v_z}{\partial x}+v_y\frac{\partial v_z}{\partial y}\right) = -\frac{\partial p}{\partial z}+\eta_0\left(\frac{\partial^2 v_z}{\partial x^2}+\frac{\partial^2 v_z}{\partial y^2}\right)+\frac{\partial S_{zx}}{\partial x}+\frac{\partial S_{zy}}{\partial y}, \tag{46}$$

where

$$\mathbf{S}=(\eta(\dot\gamma)-\eta_0)\dot{\boldsymbol\gamma}-\frac{1}{2}\Psi_1\frac{\Delta\dot{\boldsymbol\gamma}}{\Delta t}+\Psi_2\dot{\boldsymbol\gamma}.\dot{\boldsymbol\gamma}.$$

The domain of interest can be reduced to a two-dimensional space and in addition, for symmetry reasons, only a quarter of the 2D-domain, $[0,l/2]\times[0,l/2]$, is considered (Figure 4).

The pressure variable appearing in (44) and (45) is simply treated here by converting the x and y components of the velocity vector into the stream function ϕ and the vorticity ω as

$$\omega=\frac{\partial v_y}{\partial x}-\frac{\partial v_x}{\partial y}, \tag{47}$$

$$\frac{\partial\phi}{\partial y}=v_x,\quad \frac{\partial\phi}{\partial x}=-v_y. \tag{48}$$

The governing equations (44)-(46) can be reformulated into

$$\frac{\partial^2\phi}{\partial x^2}+\frac{\partial^2\phi}{\partial y^2}+\omega=0, \tag{49}$$

$$\rho\left(\frac{\partial\phi}{\partial y}\frac{\partial\omega}{\partial x}-\frac{\partial\phi}{\partial x}\frac{\partial\omega}{\partial y}\right)=\eta_0\left(\frac{\partial^2\omega}{\partial x^2}+\frac{\partial^2\omega}{\partial y^2}\right)+\frac{\partial^2 S_{xy}}{\partial x^2}-\frac{\partial^2(S_{xx}-S_{yy})}{\partial x\partial y}-\frac{\partial^2 S_{xy}}{\partial y^2}, \tag{50}$$

$$\rho\left(\frac{\partial\phi}{\partial y}\frac{\partial v_z}{\partial x}-\frac{\partial\phi}{\partial x}\frac{\partial v_z}{\partial y}\right)=-\frac{\partial p}{\partial z}+\eta_0\left(\frac{\partial^2 v_z}{\partial x^2}+\frac{\partial^2 v_z}{\partial y^2}\right)+\frac{\partial S_{zx}}{\partial x}+\frac{\partial S_{zy}}{\partial y}. \tag{51}$$

The boundary conditions for ϕ, ω and v_z are

$$\phi = 0,\ \omega = 0,\ \frac{\partial v_z}{\partial y} = 0, \qquad \text{on the line } y = 0, \tag{52}$$

$$\phi = 0,\ \omega = 0,\ \frac{\partial v_z}{\partial x} = 0, \qquad \text{on the line } x = 0, \tag{53}$$

$$\phi = 0,\ \frac{\partial \phi}{\partial y} = 0,\ v_z = 0, \qquad \text{on the line } y = \frac{l}{2}, \tag{54}$$

$$\phi = 0,\ \frac{\partial \phi}{\partial x} = 0,\ v_z = 0, \qquad \text{on the line } x = \frac{l}{2}. \tag{55}$$

The implementation of the Neumann condition $\partial v_z/\partial \bar{n}$ is similar to the previous problem. It is necessary to generate a computational boundary condition for ω at the walls $x = l/2$ and $y = l/2$ using the prescribed boundary conditions ($\partial\phi/\partial\bar{n}$). The process is as follows. In the first step, the vorticity in (49) can be simplified to be

$$\omega = -\frac{\partial^2 \phi}{\partial x^2} - \frac{\partial^2 \phi}{\partial y^2} = -\frac{\partial^2 \phi}{\partial x^2} \qquad \text{at the line } x = \frac{l}{2}, \tag{56}$$

$$\omega = -\frac{\partial^2 \phi}{\partial x^2} - \frac{\partial^2 \phi}{\partial y^2} = -\frac{\partial^2 \phi}{\partial y^2} \qquad \text{at the line } y = \frac{l}{2}. \tag{57}$$

In the second step, they are written in terms of the first-order derivatives of ϕ

$$\omega^{(i)} = = -\frac{\partial^2 \phi^{(i)}}{\partial x^2} = \sum_{j=1}^{m} \left(\mathbf{G}\mathbf{H}^{-1}_{[x]} \right)_{[i,j]} \frac{\partial \phi}{\partial x}^{(j)} \qquad \text{at the line } x = \frac{l}{2}, \tag{58}$$

$$\omega^{(i)} = = -\frac{\partial^2 \phi^{(i)}}{\partial y^2} = \sum_{j=1}^{m} \left(\mathbf{G}\mathbf{H}^{-1}_{[y]} \right)_{[i,j]} \frac{\partial \phi}{\partial y}^{(j)} \qquad \text{at the line } y = \frac{l}{2}, \tag{59}$$

and the resulting expressions (58) and (59) are then simplified by taking into account the Neumann condition $\partial\phi/\partial\bar{n}$. In the third step, the remainder of the nodal first-order derivatives of ϕ on the right-hand sides of (58) and (59) are expressed in terms of the

nodal stream function values, for example, at the boundary point $\mathbf{x^{(i)}}$,

$$\frac{\partial \phi^{(i)}}{\partial x} = \sum_{j=1}^{m} \left(\mathbf{H}_{[x]} \bar{\mathbf{H}}_{[x]}^{-1} \right)_{[i,j]} \phi^{(j)}, \tag{60}$$

$$\frac{\partial \phi^{(i)}}{\partial y} = \sum_{j=1}^{m} \left(\mathbf{H}_{[y]} \bar{\mathbf{H}}_{[y]}^{-1} \right)_{[i,j]} \phi^{(j)}. \tag{61}$$

A computational Dirichlet condition for ω is thus generated and written in terms of the nodal values of ϕ.

Three sets of uniformly distributed data points, 21×21, 26×26 and 31×31 are employed. The parameters $\partial p/\partial z$, ρ and l are chosen to be $1.0e5$ (Pa/m), 0 and 0.004 (m), respectively. The obtained results including the axial velocity, vorticity, secondary velocity vector and second normal stress difference are displayed in Figure 6, which look feasible when compared to the available solutions in the literature. To study convergence behaviour of the method, the results at the finest discretization are regarded as the "exact solutions" and the errors at coarser discretizations are then computed relative to the exact ones. Table 2 shows that errors consistently reduce with an increase in data density. It can be seen that the transverse velocity components are much smaller than the axial velocity component.

4.2 Corrugated tube flow

The steady-state axisymmetric non-Newtonian fluid flow through an undulating tube has received much attention over recent decades for a number of reasons: a) for the evaluation of constitutive equations, b) for the testing of numerical methods in non-Newtonian flow calculations and c) for the understanding of viscoelastic effects in flow through porous media [42]. In the context of numerical computation, this problem was studied by a variety of numerical methods, for example, the mixed spectral finite-difference methods (the pseudospectral/finite-difference method (PSFD), the pseudospectral cylindrical/finite-

difference method (PCFD)) [43,42,44], the full pseudospectral method (the Fourier-Chebyshev collocation method (FCC)) [45], FEM [46] and BEM [47]. The comprehensive results obtained by PSFD, PCFD and FCC can be regarded as the benchmark solutions. There is no limit point in Weissenberg number for PCFD and PSFD; their numerical calculations have shown no substantial increase of the flow resistance with increasing flow elasticity.

The local radius of an infinitely long corrugated tube is given by

$$r_w(z) = R(1 - \epsilon \sin(2\pi z/L)), \tag{62}$$

where r_w is the radius at the wall, ϵ the dimensionless amplitude of the corrugation, L the wavelength and R the mean radius of the tube (Figure 7). In addition to ϵ, another characteristic dimensionless number is the aspect ratio N, related to the dimensionless wave number l by $N = R/L = l/(2\pi)$. Owing to the fact that the flow is axisymmetric and periodic, only a reduced domain needs to be considered as shown in Figure 7.

Of interest to the experiments is the flow resistance (friction factor f times Reynolds number in the limit $Re \to 0$) defined as

$$fRe = \frac{2\pi \Delta P R^4}{L(\eta + \eta_s)Q}, \tag{63}$$

where ΔP is the pressure drop per unit cell.

The ϕ–ω formulation is adopted, where the full governing equations can be found in [48]. The Newtonian, power-law and Oldroyd-B fluid models are considered. For a power-law fluid, the stress-splitting formulation is employed.

The boundary conditions for flow in a corrugated tube are a) symmetric conditions on the centreline, b) no-slip boundary conditions on the wall and c) periodic conditions for

each dependent variable and its normal derivative on the inlet and outlet, i.e.,

$$\phi = 0,\ \omega = 0 \quad \text{(the centreline)} \tag{64}$$

$$\phi = \frac{Q}{2\pi},\ \frac{\partial \phi}{\partial \bar{n}} = 0 \ \left(\frac{\partial \phi}{\partial z} = 0, \frac{\partial \phi}{\partial r} = 0 \right) \quad \text{(the wall)} \tag{65}$$

$$\phi^i = \phi^o,\ \frac{\partial \phi^i}{\partial \bar{n}} = \frac{\partial \phi^o}{\partial \bar{n}},\ \omega^i = \omega^o,\ \frac{\partial \omega^i}{\partial \bar{n}} = \frac{\partial \omega^o}{\partial \bar{n}} \quad \text{(inlet and outlet)}, \tag{66}$$

where $\bar{n}$ is the coordinate normal to the boundary, Q the flow rate, subscripts i and o the inlet and outlet, respectively. The implementation of boundary conditions for ω on the tube wall is similar to the previous problem (flow in a square duct) and will not be repeated here.

Three data densities, namely 17×17, 21×21 and 25×25, are employed (Figure 8). Only MQs with $\beta = 1$ are implemented to study this problem.

4.2.1 Newtonian flow

Creeping flow

The unsymmetric IRBFN collocation method is first tested with the creeping flow of a Newtonian fluid. Several tube geometries are considered. The flow resistance computed by the present method is given in Table 3. Results by other methods such as FCC, PSFD, PCFD and BEM are also included for comparison. Good agreement is obtained for all test cases.

Inertial flow

Consider the inertial flow of a Newtonian fluid through a tube of $\epsilon = 0.3$ and $N = 0.16$. This flow was studied by Lahbabi and Chang [49] using the global Galerkin/spectral method and by Pilitsis and Beris [45] using the Galerkin finite element method (GFE)

and FCC for a wide range of Re from 0 to 783. For a Newtonian fluid, the nonlinearity is due to the convective term only.

Table 4 shows that errors at coarser densities, which are computed relative to the finest density, reduce with an increase in data density. The flow resistance obtained by the present method at the finest density (25×25) and those obtained by the spectral method and FEM for the above range of Re are presented in Table 5. The present results agree well with the FCC ones. Contour plots of the stream function and the vorticity fields at $Re = \{0, 22.6, 73, 397.2\}$ are displayed in Figure 9. The creeping flow field is symmetric about the widest cross section. When a Reynolds number is introduced, the symmetry is broken. Recirculation starts at a finite Reynolds number. The vortex increases in size and shifts downstream with an increase in Re.

4.2.2 Inertial flow of power-law fluid

Consider dilute aqueous solution of a polyacrylamide (Dow Separan AP-30) corresponding to 0.05% polyacrylamide concentrations by weight. The power-law parameters are given by Deiber and Schowalter [50] as $n = 0.54$ and $k = 1Ps^{n-1}$. Due to the shear-thinning form of the viscosity, there are steep boundary layers near solid boundaries, leading to difficulty in computation [42]. The flow of a power-law fluid through an undulating tube ($\epsilon = 0.3, N = 0.1592$), which was simulated by PCFD [42], is considered here.

The Reynolds number and the flow resistance for this problem are respectively defined as [42]

$$Re = \frac{2^n \pi^{n-2} \rho Q^{2-n} R^{3n-4}}{k}, \tag{67}$$

$$fRe = \frac{2^n \pi^n \Delta P R^{3n+1}}{kLQ^n}. \tag{68}$$

A decoupled approach is adopted to solve the governing equations; the nonlinearity, which arises from the viscosity function and the convective term, is treated by using a Picard's iterative scheme. Results for the flow resistance obtained by the present method are given in Table 6 together with those obtained by PCFD. The two numerical predictions show good agreement.

4.2.3 Creeping flow of Oldroyd-B fluid

A coupled approach is adopted. The nonlinearity, which arises from the convected stress derivatives, is handled by using trust region methods that retain two attractive features, namely rapid local convergence of the Newtonian iteration method and strong global convergence of the Cauchy method [51]. The boundary conditions for the stress tensor are

$$\frac{\partial S_{zz}}{\partial r} = 0,\ S_{rz} = 0, \frac{\partial S_{rr}}{\partial r} = 0,\ \frac{\partial S_{\theta\theta}}{\partial r} = 0 \quad \text{(the centreline)} \tag{69}$$

$$S^i_{zz} = S^o_{zz},\ \frac{\partial S^i_{zz}}{\partial \bar{n}} = \frac{\partial S^o_{zz}}{\partial \bar{n}},\ S^i_{rz} = S^o_{rz},\ \frac{\partial S^i_{rz}}{\partial \bar{n}} = \frac{\partial S^o_{rz}}{\partial \bar{n}} \cdots \text{(inlet and outlet)}. \tag{70}$$

A Weissenberg number is defined as [43]

$$We = \frac{\lambda Q}{R^3}. \tag{71}$$

Along the wall of a tube, all convected stress derivatives vanish, and hence the constitutive equations are reduced to algebraic equations which can be easily solved pointwise for the unknown stress tensor.

Along the centreline, the dependent variables will be determined here by imposing the symmetric conditions directly on the corresponding networks rather than using the usual L'Hopital's rule or a simplified form of the governing equations. The detailed implementation is as follows.

As mentioned earlier, all variables and their derivatives in the present procedure are expressed as linear combinations of the nodal variable values over the whole domain. Let f be a dependent variable. The first-order derivative of f with respect to r along the centreline can be written as

$$\mathbf{f}_{,\mathbf{r}}{}^{c} = \mathbf{H}^{c}_{[r]}\bar{\mathbf{H}}^{-1}_{[r]}\mathbf{f}, \tag{72}$$

where subscript c denotes the centreline. Making use of the symmetric conditions, (72) becomes

$$\mathbf{0} = \mathbf{H}^{c}_{[r]}\bar{\mathbf{H}}^{-1}_{[r]}\mathbf{f}. \tag{73}$$

By solving (73), the centreline values of f can be expressed in terms of the remainder of the nodal values of f. A variable f can be v_z, S_{zz}, S_{rr} or $S_{\theta\theta}$. With this treatment, one can avoid to solve ordinary differential equations that are associated with a simplified form of constitutive equations or to compute higher-order derivatives that are associated with L'Hopital's rule. Note that higher-order derivatives lead to larger errors in the context of function approximation.

Moderate corrugation amplitude and moderate wavelength ($\epsilon = 0.1,\ N = 0.16$)

The retardation defined as $\alpha = \eta/(\eta_s + \eta)$ is chosen to be 0.15, which was used in [43]. Convergence can be obtained up to high values of the Weissenberg number, at least of about 30 (Figure 10). For the range of We from 0 to 20, the flow resistance does not differ substantially from that obtained at $We = 0$ (Newtonian fluid), which looks feasible when compared to the available results in the literature. However, the present flow resistance is observed to increase quickly when $We > 20$. The reason could be that data densities become too coarse to accurately capture the solution, especially for the stress fields near boundaries.

Moderate corrugation amplitude and small wavelength ($\epsilon = 0.1,\ N = 0.5$)

The flow of an Oldroyd-B fluid through an undulating tube ($\epsilon = 0.1,\ N = 0.5$) was

simulated by FCC [45], where the flow resistance values were tabulated at two Weissenberg numbers, $We = 1.2071$ and $We = 3.6213$. They are used here for comparison. Numerical predictions by FCC and IRBFN are in good agreement as shown in Figure 11. Like the previous case ($\epsilon = 0.1,\ N = 0.16$), there is a substantial increase in the present fRe when the Weissenberg number is greater than a certain value (about of 5 here). Thus, this We value is considered as a limit of the IRBFN approach using the present data densities.

4.2.4 Comparison with FCC

In an effort to ease the large computational costs that are required by PSFD and PCFD, Pilitsis and Beris [45] developed a full pseudospectral method, namely the Fourier-Chebyshev collocation (FCC) technique, for computing the steady-state axisymmetric non-Newtonian fluid flow in a periodically constricted tube. In FCC, the radial dependence of the variables are approximated by using Chebyshev polynomials, while the dependence on the axial coordinate are approximated by Fourier sine and cosine functions. The FCC yielded highly accurate solutions using low numbers of data points. The computational costs are relatively low for coarse discretizations, but become very expensive for fine discretizations due to the full structure of large Jacobian matrices.

The present IRBFN method appears to be close to the FCC method in the sense a) they are global high-order methods, b) the governing equations are approximated in the strong form by point collocation and c) the resultant matrices are dense.

In contrast to the FCC method, the present method uses only IRBFNs to represent the field variables and their derivatives in the radial and axial directions. Furthermore, collocation points in the IRBFN method can be chosen randomly, while the coordinates of data points in the radial direction in the FCC method should be chosen as the roots of Chebyshev polynomials (Note that the use of cosine-type points in FCC allows a fast Fourier transform to be used to shift between spectral space and physical space; the

IRBFN method has no such rapid matrix computations). The present method can be extended to non-periodic flows or irregular domains straightforwardly.

5 Concluding remarks

This paper reports a numerical method based on RBFNs for solving non-Newtonian fluid flow problems. The main advantages of the present method are its mesh-free nature and easy implementation. IRBFNs are employed to represent the solution variables; the multiple spaces of network weights are converted into the single space of nodal variable values. In the case that the viscosity function depends on the rate of deformation, stress-splitting techniques are utilized to enhance numerical stability. Stabler and faster convergence is obtained with the chosen viscosity being the average value of the viscosity field of the previous iteration. The method is verified through the simulation of flows of inelastic and viscoelastic fluids in a straight duct and in an undulating tube that are induced by axial pressure drop. The results are compared with the analytic and benchmark solutions; good agreement is achieved. The main disadvantage of the method is the large computational requirement imposed because of the involvement of dense matrices. The implementation of a local meshless version and how to treat convected stress derivatives effectively with IRBFNs will be investigated in future studies.

ACKNOWLEDGEMENT

The authors would like to acknowledge the computing facilities provided by the APAC National Facilities. N. Mai-Duy also wishes to thank the University of Sydney for a Sesqui Postdoctoral Research Fellowship. The authors gratefully acknowledge helpful comments from the referees.

REFERENCES

1. Jin X, Li G, Aluru NR. On the equivalence between least-squares and kernel approximations in meshless methods. *Computer Modeling in Engineering and Sciences* 2001; **2**(4): 447–462.

2. Li S, Liu WK. Meshfree and particle methods and their applications. *Applied Mechanics Reviews* 2002; **55**(1): 1–34.

3. Atluri SN, Shen S. *The Meshless Local Petrov-Galerkin Method*. Tech Science Press: Encino, 2002.

4. Liu GR. *Mesh Free Methods: Moving beyond the Finite Element Method*. CRC Press: Boca Raton, 2003.

5. Lucy LB. A numerical approach to the testing of the fission hypothesis. *The Astronomical Journal* 1977; **8**: 1013–1024.

6. Liu WK, Jun S, Zhang Y. Reproducing kernel particle methods. *International Journal for Numerical Methods in Fluids* 1995; **20**: 1081–1106.

7. Atluri SN, Zhu T. A new meshless local Petrov-Galerkin (MLPG) approach in computational mechanics. *Computational Mechanics* 1998; **22**: 117–127.

8. Liu GR, Gu YT. A local radial point interpolation method (LRPIM) for free vibration analyses of 2-D solids. *Journal of Sound and Vibration* 2001; **246**(1): 29–46.

9. Belytschko T, Lu YY, Gu L. Element-free Galerkin methods. *International Journal for Numerical Methods in Engineering* 1994; **37**: 229–256.

10. Kansa EJ. Multiquadrics—A scattered data approximation scheme with applications to computational fluid-dynamics—I. Surface approximations and partial derivative estimates. *Computers and Mathematics with Applications* 1990; **19**(8/9): 127–145.

11. Mai-Duy N, Tran-Cong T. Approximation of function and its derivatives using radial basis function network methods. *Applied Mathematical Modelling* 2003; **27**: 197–220.

12. Kansa EJ. Multiquadrics—A scattered data approximation scheme with applications to computational fluid-dynamics—II. Solutions to parabolic, hyperbolic and elliptic partial differential equations. *Computers and Mathematics with Applications* 1990; **19**(8/9): 147–161.

13. Franke C, Schaback R. Solving partial differential equations by collocation using radial basis functions. *Applied Mathematics and Computation* 1998; **93**: 73–82.

14. Kansa EJ, Hon YC. Circumventing the ill-conditioning problem with multiquadric radial basis functions: applications to elliptic partial differential equations. *Computers and Mathematics with Applications* 2000; **39**: 123–137.

15. Mai-Duy N, Tran-Cong T. Numerical solution of differential equations using multiquadric radial basis function networks. *Neural Networks* 2001; **14**(2): 185–199.

16. Larsson E, Fornberg B. A numerical study of some radial basis function based solution methods for elliptic PDEs. *Computers and Mathematics with Applications* 2003; **46**: 891–902.

17. Zerroukat M, Power H, Chen CS. A numerical method for heat transfer problems using collocation and radial basis functions. *International Journal for Numerical Methods in Engineering* 1998; **42**: 1263–1278.

18. Zerroukat M, Djidjeli K, Charafi A. Explicit and implicit meshless methods for linear advection-diffusion-type partial differential equations. *International Journal for Numerical Methods in Engineering* 2000; **48**: 19–35.

19. Mai-Duy N. Solving high order ordinary differential equations with radial basis function networks. *International Journal for Numerical Methods in Engineering*

2005; **62**: 824–852.

20. Mai-Duy N, Tanner RI. Solving high order partial differential equations with radial basis function networks. *International Journal for Numerical Methods in Engineering* 2005; (accepted).

21. Leitao V. A meshless method for Kirchhoff plate bending problems. *International Journal for Numerical Methods in Engineering* 2001; **52**(10): 1107–1130.

22. Mai-Duy N, Tran-Cong T. Numerical solution of Navier-Stokes equations using multiquadric radial basis function networks. *International Journal for Numerical Methods in Fluids* 2001; **37**: 65–86.

23. Shu C, Ding H, Yeo KS. Local radial basis function-based differential quadrature method and its application to solve two-dimensional incompressible Navier-Stokes equations. *Computer Methods in Applied Mechanics and Engineering* 2003; **192**: 941–954.

24. Tanner RI. *Engineering Rheology*. Oxford University Press: New York, 2000.

25. Haykin S. *Neural Networks: A Comprehensive Foundation*. Prentice-Hall: New Jersey, 1999.

26. Micchelli CA. Interpolation of scattered data: distance matrices and conditionally positive definite functions. *Constructive Approximation* 1986; **2**: 11–22.

27. Park J, Sandberg IW. Universal approximation using radial basis function networks. *Neural Computation* 1991; **3**: 246–257.

28. Cover TM. Geometrical and statistical properties of systems of linear inequalities with applications in pattern recognition. *IEEE Transactions on Electronic Computers* 1965; **EC-14**: 326–334.

29. Young DM, Wheeler MF. Alternating direction methods for solving partial difference equations. In *Nonlinear Problems of Engineering*, Ames WF (ed); Academic Press: New York, 1964; pp. 220–246.

30. Hartnett JP, Kostic M. Heat transfer to Newtonian and non-Newtonian fluids in rectangular ducts. *Advances in Heat Transfer* 1989; **19**: 247–356.

31. Schechter RS. On the steady flow of a non-Newtonian fluid in cylinder ducts. *A.I.Ch.E Journal* 1961; **7**: 445–448.

32. Wheeler JA, Wissler EH. The friction factor-Reynolds number relation for the steady flow of pseudoplastic fluids through rectangular ducts. *A.I.Ch.E Journal* 1965; **11**(2): 207–216.

33. Syrjala S. Finite-element analysis of fully developed laminar flow of power-law non-Newtonian fluid in a rectangular duct. *International Communications in Heat and Mass Transfer* 1995; **22**(4): 549–557.

34. Kozicki W, Chou CH, Tiu C. Non-Newtonian flow in ducts of arbitrary cross-section shape. *Chemical Engineering Science* 1966; **21**: 665–679.

35. Green AE, Rivlin RS. Steady flow of non-Newtonian fluids through tubes. *Quarterly of Applied Mathematics* 1956; **14**: 299–308.

36. Langlois WE, Rivlin RS. Slow steady-state flow of visco-elastic fluids through non–circular tubes. *Rendiconti di Matematica* 1963; **22**: 169–185.

37. Townsend P, Walters K, Waterhouse WM. Secondary flows in pipes of square cross-section and the measurement of the second normal stress difference. *Journal of Non-Newtonian Fluid Mechanics* 1976; **1**: 107–123.

38. Gervang B, Larsen PS. Secondary flows in straight ducts of rectangular cross section. *Journal of Non-Newtonian Fluid Mechanics* 1991; **39**: 217–237.

39. Xue S-C, Phan-Thien N, Tanner RI. Numerical study of secondary flows of viscoelastic fluid in straight pipes by an implicit finite volume method. *Journal of Non-Newtonian Fluid Mechanics* 1995; **59**: 191–213.

40. Gao SX, Hartnett JP. Steady flow of non-Newtonian fluids through rectangular ducts. *International Communications in Heat and Mass Transfer* 1993; **20**: 197–210.

41. Debbaut B, Avalosse T, Dooley J, Hughes K. On the development of secondary motions in straight channels induced by the second normal stress difference: experiments and simulations. *Journal of Non-Newtonian Fluid Mechanics* 1997; **69**: 255–271.

42. Pilitsis S, Souvaliotis A, Beris AN. Viscoelastic flow in a periodically constricted tube: the combined effect of inertia, shear thinning and elasticity. *Journal of Rheology* 1991; **35**(4): 605–646.

43. Pilitsis S, Beris AN. Calculations of steady-state viscoelastic flow in an undulating tube. *Journal of Non-Newtonian Fluid Mechanics* 1989; **31**: 231–287.

44. Pilitsis S, Beris AN. Viscoelastic flow in an undulating tube. Part II. Effects of high elasticity, large amplitude of undulation and inertia. *Journal of Non-Newtonian Fluid Mechanics* 1991; **39**: 375–405.

45. Pilitsis S, Beris AN. Pseudospectral calculations of viscoelastic flow in a periodically constricted tube. *Computer Methods in Applied Mechanics and Engineering* 1992; **98**: 307–328.

46. Burdette SR, Coates PJ, Armstrong RC, Brown RA. Calculations of viscoelastic flow through an axisymmetric corrugated tube using the explicitly elliptic momentum equation formulation (EEME). *Journal of Non-Newtonian Fluid Mechanics* 1989; **33**: 1–23.

47. Zheng R, Phan-Thien N, Tanner RI, Bush MB. Numerical analysis of viscoelastic flow through a sinusoidally corrugated tube using a boundary element method. *Journal of Rheology* 1990; **34**(1): 79–102.

48. Crochet MJ, Davies AR, Walters K. *Numerical Simulation of Non-Newtonian Flow*. Elsevier: Amsterdam, 1984.

49. Lahbabi A, Chang H-C. Flow in periodically constricted tubes: transition to inertial and nonsteady flows. *Chemical Engineering Science* 1985; **41**(10): 2487–2505.

50. Deiber JA, Schowalter WR. Modeling the flow of viscoelastic fluids through porous media. *A.I.Ch.E Journal* 1981; **27**(6): 912–920.

51. McCartin BJ. A model-trust region algorithm utilizing a quadratic interpolant. *Journal of Computational and Applied Mathematics* 1998; **91**: 249–259.

Table 1: Rectilinear flow of power-law fluid in a square duct: comparison of the friction factor fRe between the IRBFN method using 27×27 data points and other methods. All predictions are in good agreement over a wide range of n.

	fRe				
n	IRBFN	Variational [31]	FDM [32]	General expression [34]	FEM [33]
1.0	14.22	14.27	14.22	14.21	14.22
0.9	11.88		11.90	11.96	11.88
0.8	9.91		9.91	10.06	9.91
0.7	8.26		8.26	8.45	8.26
0.6	6.88		6.88	7.08	6.88
0.5	5.72	5.755	5.72	5.93	5.72
0.4	4.74		4.74	4.95	4.74
0.3	3.91			4.11	3.91
0.2	3.17			3.38	3.19

Table 2: Non-rectilinear flow of CEF fluid in a square duct: the extreme values of the velocity components and the stream function.

Density	$(v_z)_{max}$(error)	$(\sqrt{v_x^2 + v_y^2})_{max}$	$(\phi)_{min}$(error)	$(\phi)_{max}$(error)
21×21	567.8(0.33%)	4.1	-1.245(1.03%)	1.245(1.03%)
26×26	569.5(0.03%)	4.1	-1.256(0.15%)	1.256(0.15%)
31×31	569.7	4.1	-1.258	1.258

Table 3: "Wiggly" tube problem, Newtonian fluid, $Re = 0.0$, 25×25: the computed flow resistance by the present method and other methods for several geometries. Good agreement is achieved for all cases. Note that Pertb. denotes Perturbation analysis; GSM—Galerkin spectral method; [a]—[47]; [b]—[43]; [c]—[49].

	fRe				
Method	$\epsilon = 0.1$ $N = 0.5$	$\epsilon = 0.2$ $N = 0.1042$	$\epsilon = 0.2$ $N = 0.5$	$\epsilon = 0.3$ $N = 0.1592$	$\epsilon = 0.286$ $N = 0.2333$
IRBFN	17.7480	19.7582	23.2883	26.4331	26.3814
BEM[a]	17.7346	19.7268	23.2253	26.3759	26.3285
FCC[b]	$\cdots$	19.7655	$\cdots$	26.437	26.383
PSFD[b]	17.75	19.765	$\cdots$	26.436	26.383
PCFD[b]	17.75	17.761	23.28	26.432	26.377
FEM[b]	$\cdots$	19.756	$\cdots$	26.385	26.293
Pertb.[a]	17.85	19.38	23.41	24.16	24.42
GSM[c]	$\cdots$	19.76	$\cdots$	26.40	25.85

Table 4: "Wiggly" tube problem ($\epsilon = 0.3; N = 0.16$), Newtonian fluid: the computed flow resistance by the IRBFN method for a wide range of Re.

Re	fRe (Error %)		
	17×17	21×21	25×25
0.0	26.4548 (0.0389)	26.4462 (0.0064)	26.4445
0.012	26.4548 (0.0389)	26.4462 (0.0064)	26.4445
12.0	27.1968 (0.0718)	27.1814 (0.0151)	27.1773
22.6	28.5797 (0.0918)	28.5594 (0.0207)	28.5535
51.0	31.7581 (0.0220)	31.7569 (0.0183)	31.7511
73.0	33.4312 (0.0676)	33.4583 (0.0135)	33.4538
132.0	36.4210 (0.3322)	36.5485 (0.0167)	36.5424
207.4	38.6855 (0.8054)	39.0200 (0.0523)	38.9996
264.0	39.7736 (1.3170)	40.3439 (0.0980)	40.3044
397.2	41.1336 (3.1227)	42.5737 (0.2690)	42.4595
783.0	—	46.0876 (0.7595)	45.7402

Table 5: "Wiggly" tube problem ($\epsilon = 0.3; N = 0.16$), Newtonian fluid: comparison of the flow resistance for a wide range of Re between the present method and other methods. Good agreement is shown for the whole range of Re. The IRBFN method has better agreement with the FCC. Note that GFE denotes the Galerkin finite element method; GSM—Galerkin spectral method; ^{a}—[45]; N_x, N_c—the number of Fourier, Chebyshev modes in the axial and stretched radial directions, respectively; and N_r, N_z—the number of elements in the r and z directions, respectively.

	fRe			
Re	IRBFN 25×25	GSM[a]	FCC[a] $N_x = 16, N_c = 33$	GFE[a] $N_r = 40, N_z = 40$
0.0	26.4445	26.4	26.4484	26.4193
0.012	26.4445	26.4	26.4484	26.4193
12.0	27.1773	27.1	27.1791	27.0911
22.6	28.5535	28.5	28.5536	28.4433
51.0	31.7511	31.7	31.7484	31.6984
73.0	33.4538	33.4	33.4488	33.4039
132.0	36.5424	36.7	36.5264	36.5392
207.4	38.9996	38.9	38.9607	38.9330
264.0	40.3044	39.7	40.2446	40.1544
397.2	42.4595	40.6	42.3479	42.1112
783.0	45.7402	41.2	45.5828	45.0734

Table 6: "Wiggly" tube problem ($\epsilon = 0.3; N = 0.1592$), power-law model ($n = 0.54; k = 1.0$): the computed flow resistance by IRBFN and PCFD for a wide range of Re. The IRBFN results agree well with the PCFD results. Note that N_x, N_p denote the numbers of Fourier mode and finite difference points in the axial and stretched radial directions, respectively and [a]—[42].

	fRe	
Re	IRBFN 25×25	PCFD[a] $N_x = 16, N_p = 100$
0.0	9.1268	9.1052
1.528	9.1434	9.1240
12.484	9.8270	9.8508
21.581	10.3788	10.3885
36.912	11.0120	11.0083
50.430	11.4189	11.3988
62.905	11.7202	11.6876
85.934	12.1586	12.1067

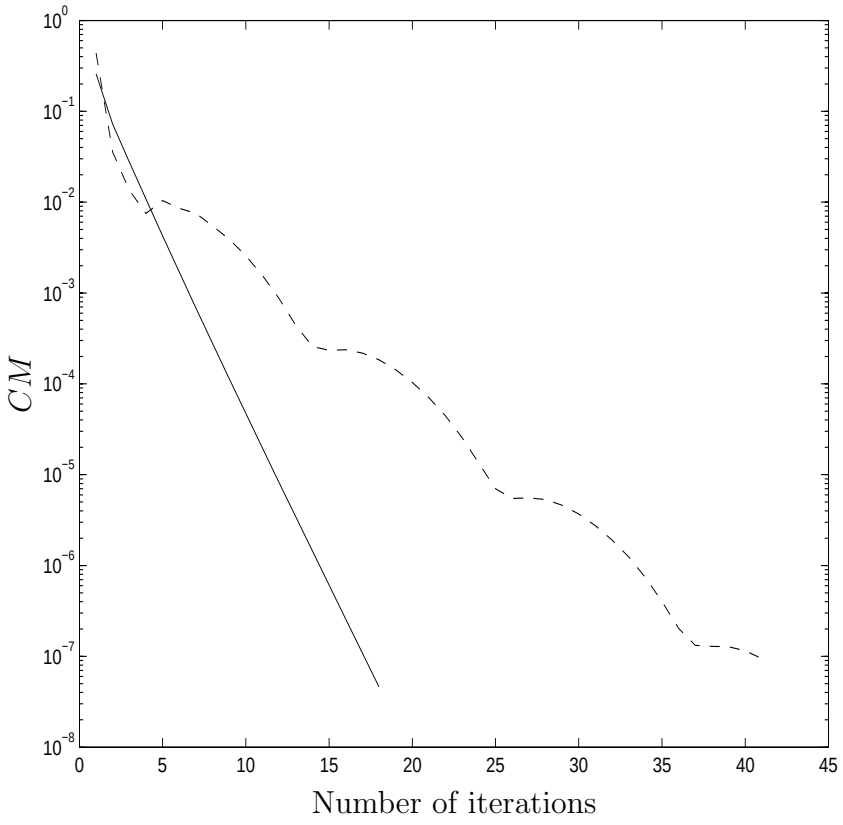

Figure 1: Rectilinear flow of power-law fluid in a straight pipe, $k = 1$, $\partial p/\partial z = -1$, $n = 0.75$, $\alpha = 1$, 13 data points: comparison of convergence behaviour of the iterative procedure between two cases $\eta_0 = \bar{\eta}$ (solid line) and $\eta_0 = \eta_N$ (dashed line). The former converges much faster and is stabler than the latter.

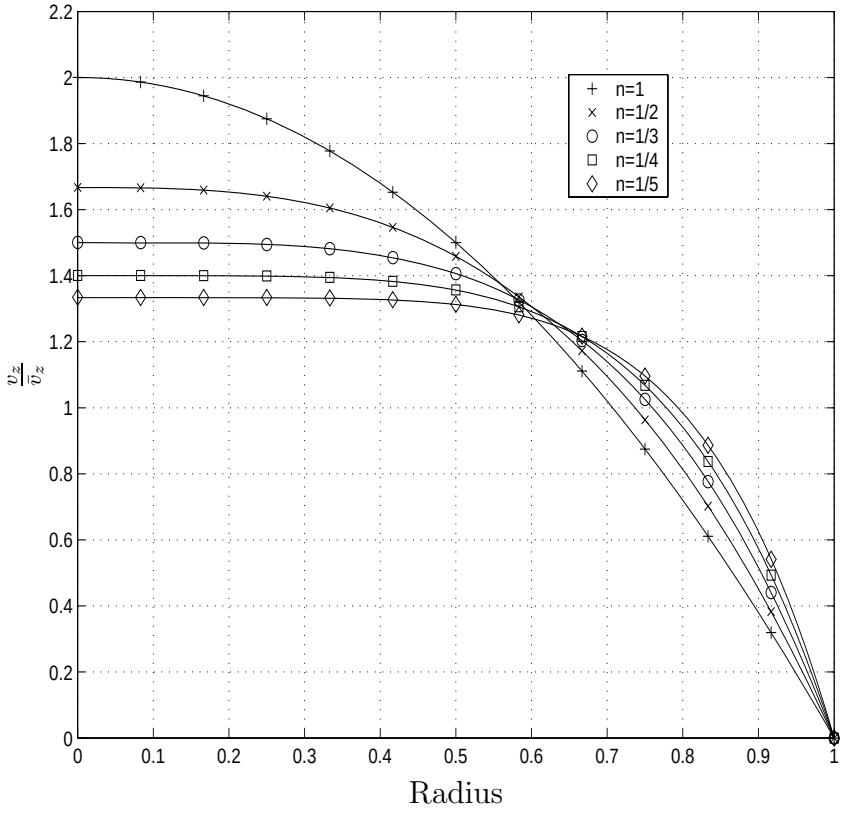

Figure 2: Rectilinear flow of power-law fluid in a straight pipe, $k = 1$, $\partial p/\partial z = -1$: the computed velocity profiles for a wide range of n using 13 collocation points. Good agreement is shown between the computed and the exact (solid line) solutions for all values of n.

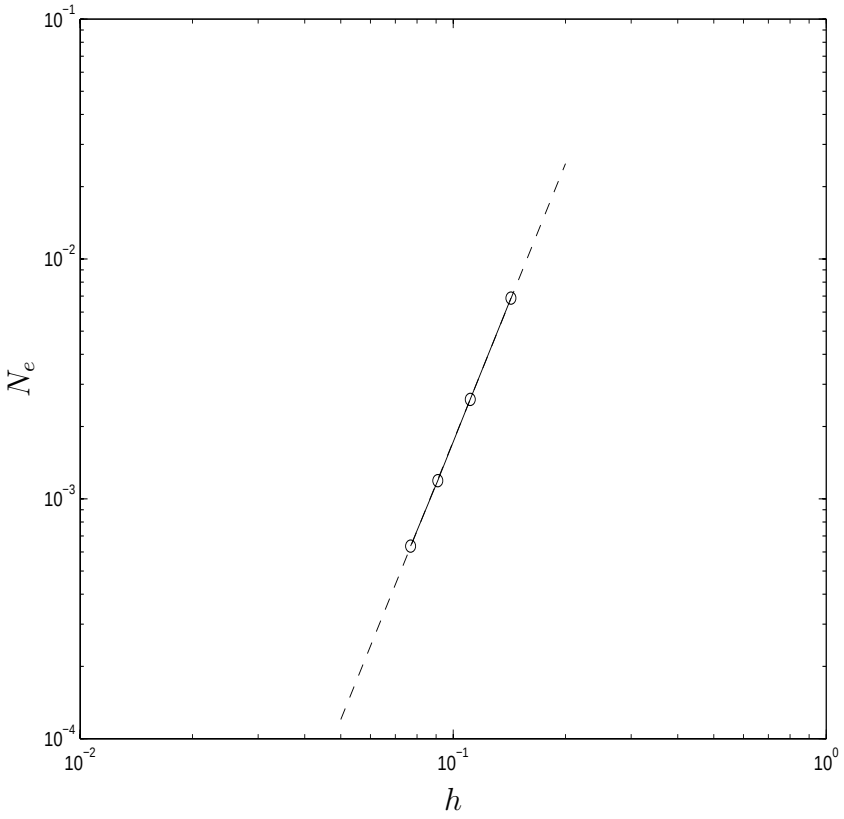

Figure 3: Rectilinear flow of power-law fluid in a straight pipe, $k = 1$, $\partial p/\partial z = -1$, $n = 1/5$: convergence rate. The IRBFN solution converges apparently as $O(h^{3.85})$, where h is the data point spacing.

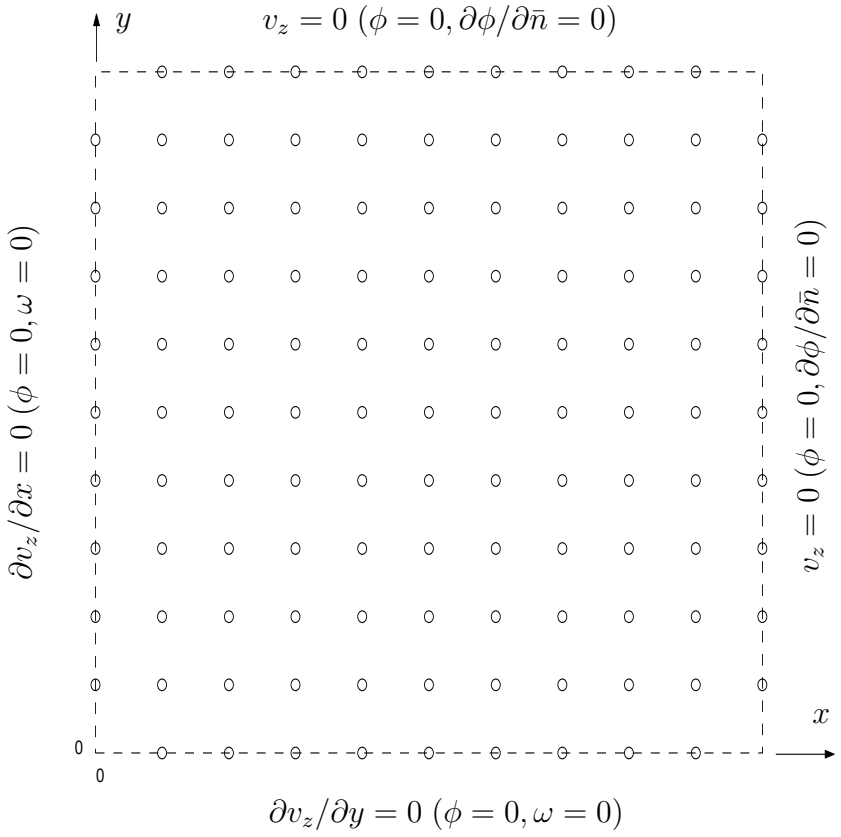

Figure 4: Power law and CEF fluids flowing through a square duct: domain of interest, discretization and boundary conditions (v_z: power law fluid, rectilinear flow; $v_z, \phi, \omega, \partial\phi/\partial\bar{n}$: CEF fluid, non-rectilinear flow). The problem domain is simply represented by a set of discrete points instead of a set of elements.

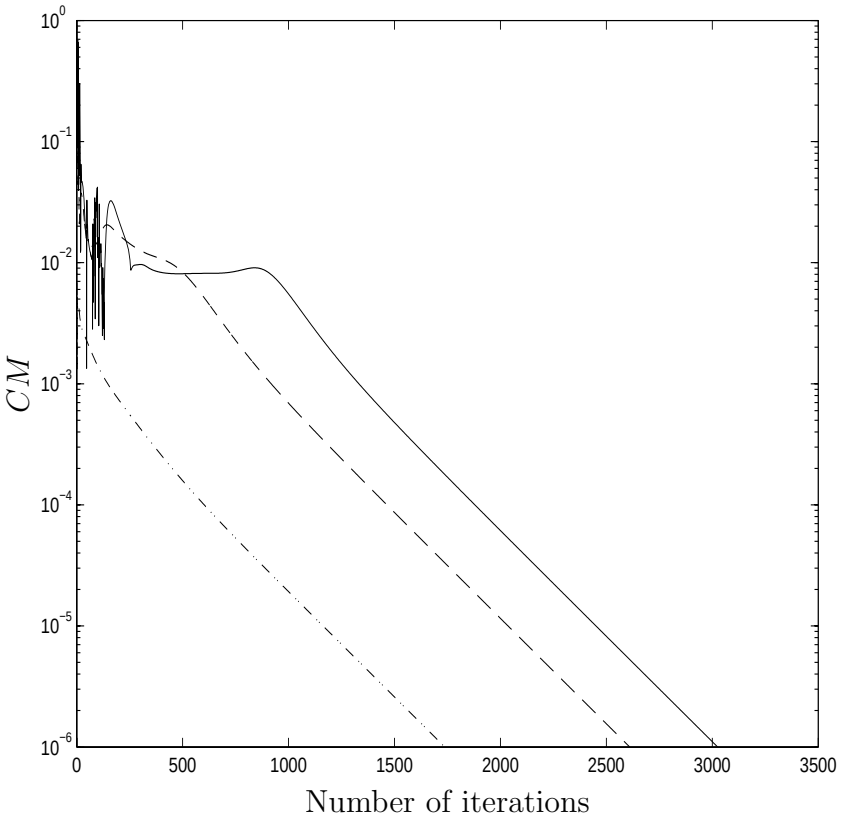

Figure 5: Rectilinear flow of power-law fluid in a square duct, $k = 1$, $\partial p/\partial z = -1$, $n = 1/5$, $\alpha = 0.3$, data density of 11×11: effect of an initial solution on convergence. The computed solutions at higher values of n are used as initial solutions (solid line: $n = 1$, dashed line: $n = 1/2$, and dashdot line: $n = 1/4$). It is relatively difficult to obtain convergence for $n = 1/5$ as a large number of iteration is required. A closer initial solution yields faster convergence.

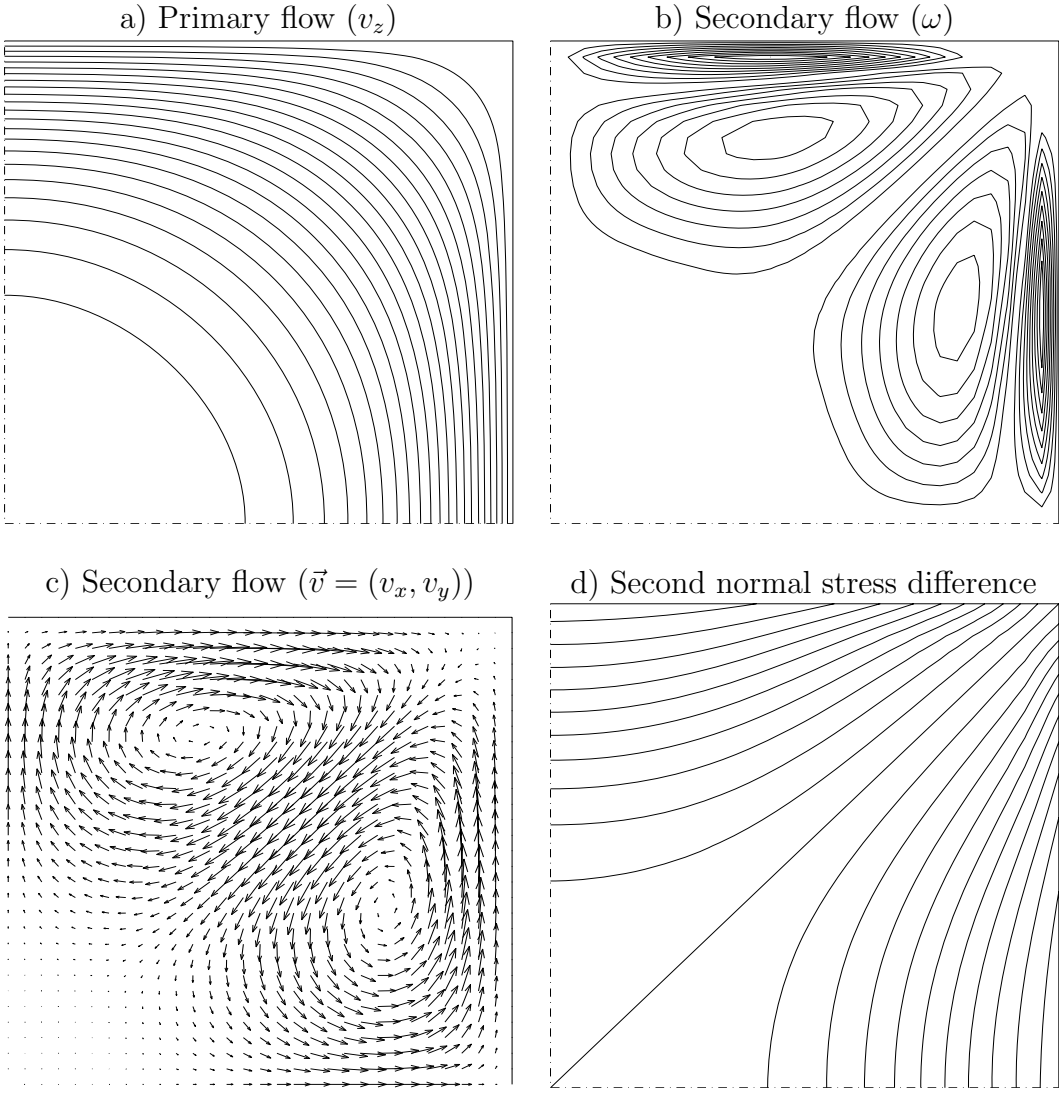

Figure 6: Non-rectilinear flow of CEF fluid in a square duct, data density of 31×31: some contour plots.

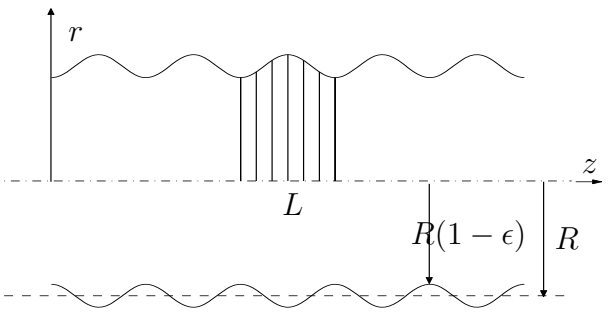

Figure 7: "Wiggly" tube problem: geometry. The shaded area represents a unit computation cell.

a) 17×17 data points

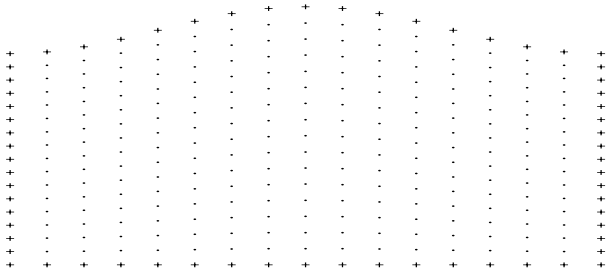

c) 21×21 data points

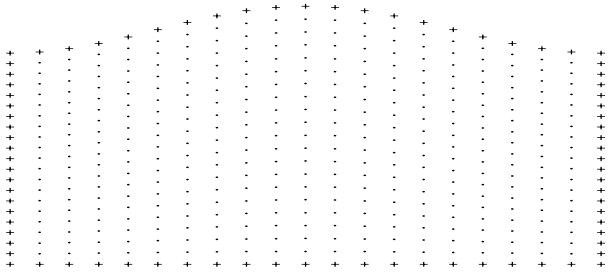

b) 25×25 data points

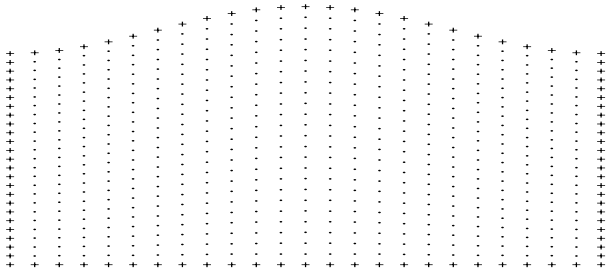

Figure 8: "Wiggly" tube problem: computational domain and discretizations. Legends: (+) boundary point, (.) interior point. The problem domain is simply represented by a set of discrete points instead of a set of elements.

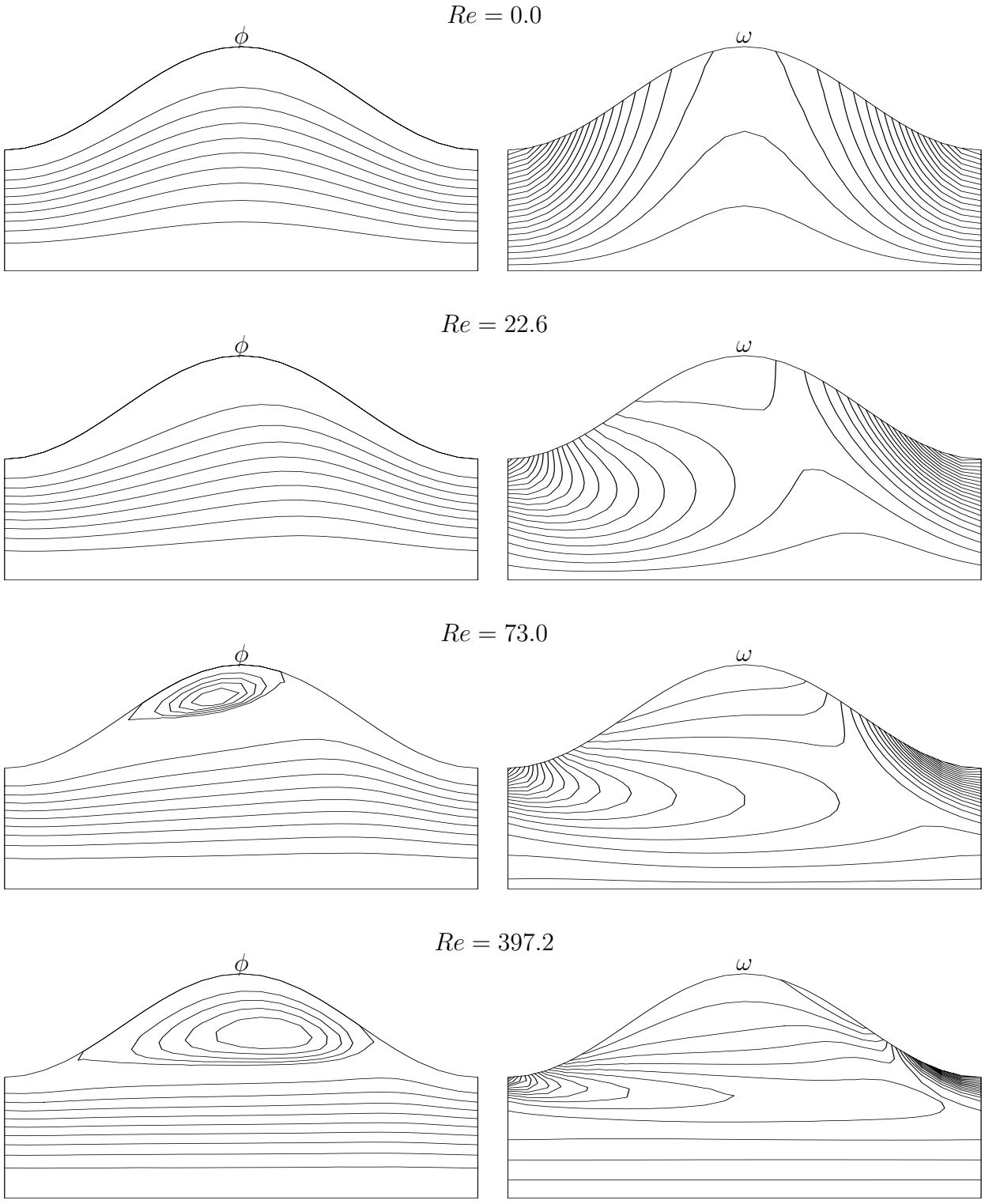

Figure 9: "Wiggly" tube problem, $\epsilon = 0.3$, $N = 0.16$, 25×25, Newtonian fluid: contour plots of the stream function ϕ and the vorticity ω for several Res.

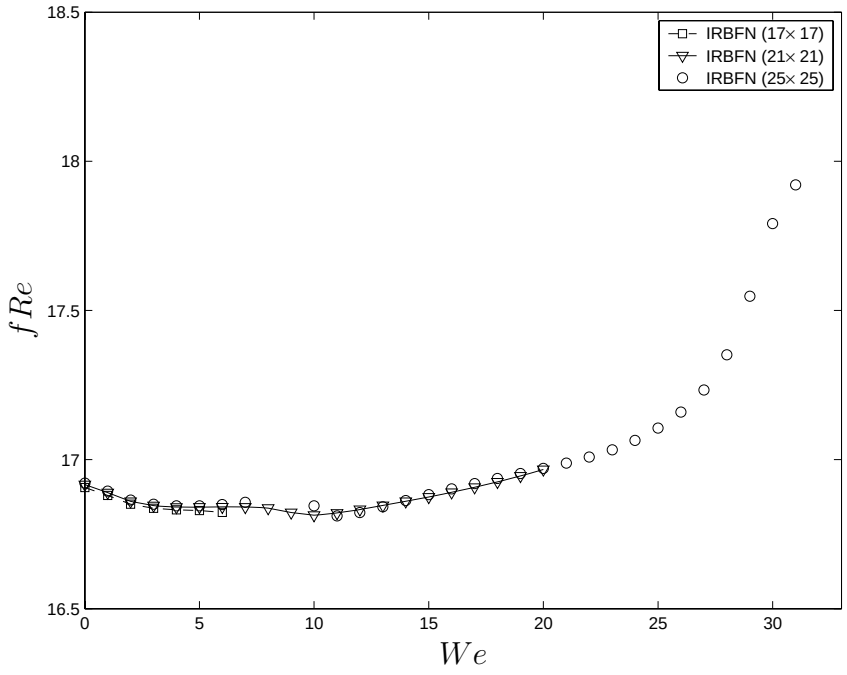

Figure 10: "Wiggly" tube problem, $\epsilon = 0.1$, $N = 0.16$, Oldroyd-B fluid: the plot of flow resistance (fRe) versus Weissenberg number (We) for three discretizations (17×17, 21×21 and 25×25).

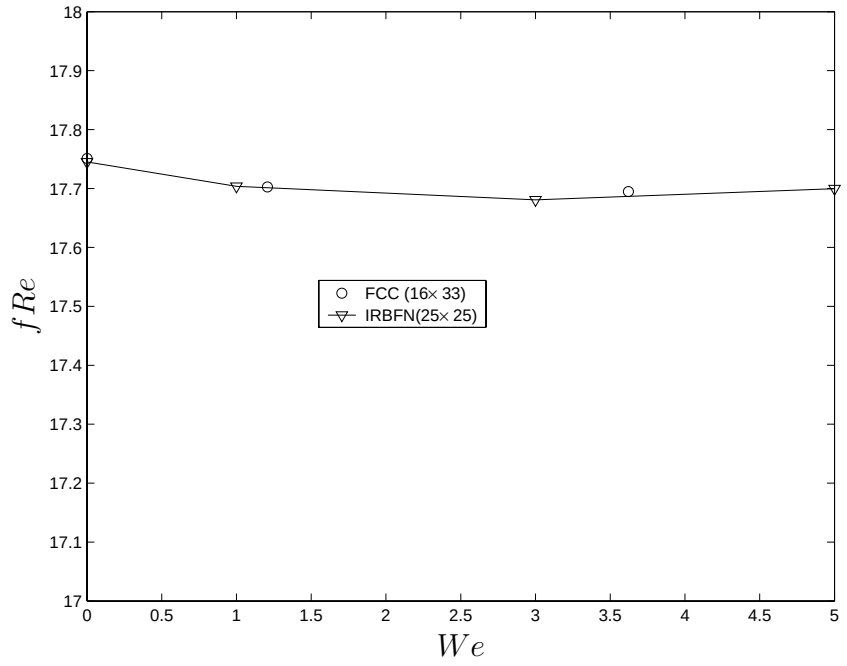

Figure 11: "Wiggly" tube problem, $\epsilon = 0.1$, $N = 0.5$, Oldroyd-B fluid: Comparison of the flow resistance obtained by IRBFN and FCC [45]. The two numerical predictions are in good agreement.